

Small compressive strain induced semiconductor-metal transition and tensile strain enhanced thermoelectric properties in monolayer PtTe₂

San-Dong Guo

Department of Physics, School of Sciences, China University of Mining and Technology, Xuzhou 221116, Jiangsu, China

Biaxial strain effects on electronic structures and thermoelectric properties of monolayer PtTe₂ are investigated by using generalized gradient approximation (GGA) plus spin-orbit coupling (SOC) for the electron part and GGA for the phonon part. Calculated results show that small compressive strain (about -3%) can induce semiconductor-to-metal transition, which can easily be achieved in experiment. The conduction bands convergence is observed for unstrained PtTe₂, which can be removed by both compressive and tensile strains. Tensile strain can give rise to valence bands convergence by changing the position of valence band maximum (VBM), which can induce enhanced Seebeck coefficient, being favorable for high power factor. It is found that tensile strain can also reduce lattice thermal conductivity, which at the strain of 4% can decrease by about 19% compared to unstrained one at room temperature. By considering tensile strain effects on ZT_e and lattice thermal conductivity, tensile strain indeed can improve p-type efficiency of thermoelectric conversion. Our results demonstrate the potential of strain engineering in PtTe₂ for applications in electronics and thermoelectricity.

PACS numbers: 72.15.Jf, 71.20.-b, 71.70.Ej, 79.10.-n
Keywords: Strain; semiconductor-metal transition; Power factor; lattice thermal conductivity

Email: guosd@cumt.edu.cn

I. INTRODUCTION

Due to potential application in electronic and energy conversion devices, two-dimensional (2D) materials have been widely investigated both in theory and experiment¹⁻⁴. Since the discovery of graphene, great efforts have been made to explore 2D materials, such as hexagonal boron nitride⁵, germanene, silicene⁶, phosphorene⁷, group IV-VI compounds⁸ and transition metal dichalcogenides⁹. The transition metal dichalcogenides monolayer MoS₂ possesses intrinsic direct band gap of 1.9 eV in comparison with the gapless Graphene, and has been applied in field effect transistors, photovoltaics and photocatalysis¹⁰⁻¹². The thermoelectric properties related with MoS₂ have also been widely investigated¹³⁻¹⁶, and the dimensionless figure of merit, $ZT = S^2\sigma T/(\kappa_e + \kappa_L)$, can measure efficiency of thermoelectric conversion, in which S , σ , T , κ_e and κ_L are the Seebeck coefficient, electrical conductivity, absolute temperature, the electronic and lattice thermal conductivities, respectively. The strain engineering is a very effective approach to tune band structure and transport properties in MoS₂¹⁷⁻¹⁹.

Recently, the transition metal dichalcogenides monolayer PtSe₂ has been epitaxially grown with high-quality single-crystal, and the local Rashba spin polarization and spin-layer locking are proved by spin- and angle-resolved photoemission spectroscopy, which has potential applications in electrically tunable spintronics and valleytronics^{20,21}. Biaxial strain effects on electronic structures and thermoelectric properties in monolayer PtSe₂ have also been investigated^{22,23}, and tensile strain can improve thermoelectric properties by enhancing power factor ($S^2\sigma$) and reducing lattice thermal conductivity (κ_L). Among PtX₂ (X=S, Se and Te), PtTe₂ has the smallest energy band gap²⁴, which means small

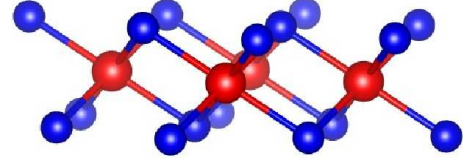


FIG. 1. (Color online) A sketch map of crystal structure of monolayer PtTe₂. The large red balls represent Pt atoms, and small blue balls are Te atoms.

strain may induce semiconductor-metal transition, and has the largest lattice constant a^{24} , which implies low lattice thermal conductivity according to tensile strain reduced lattice thermal conductivity in PtSe₂²³.

Here, we investigate biaxial strain dependence of electronic structures and thermoelectric properties of monolayer PtTe₂ by first-principle calculations and Boltzmann transport theory. The SOC has important effects on electronic structures and power factors in semiconducting transition-metal dichalcogenide monolayers^{19,23,24}, so the electron part is performed using GGA+SOC, while the lattice part is calculated using GGA. It is found that energy band gap first increases, and then decreases from compressive strain to tensile strain, which is in excellent agreement with strain dependence of energy band gap of other semiconducting transition-metal dichalcogenide monolayers, such as MoS₂^{17,19} and PtSe₂^{22,23}. Calculated results show that the spin-orbit splitting at Γ point, Se-Te bond length and Se-Pt-Te bond angle monotonically decrease, while Pt-Te bond length monotonically increases. Compressive strain can easily induce semiconductor-metal transition as a result of enhanced orbital overlap and hybridization. Tensile strain can induce valence bands convergence by valley degeneracies, leading to improved Seebeck coefficient, and then can

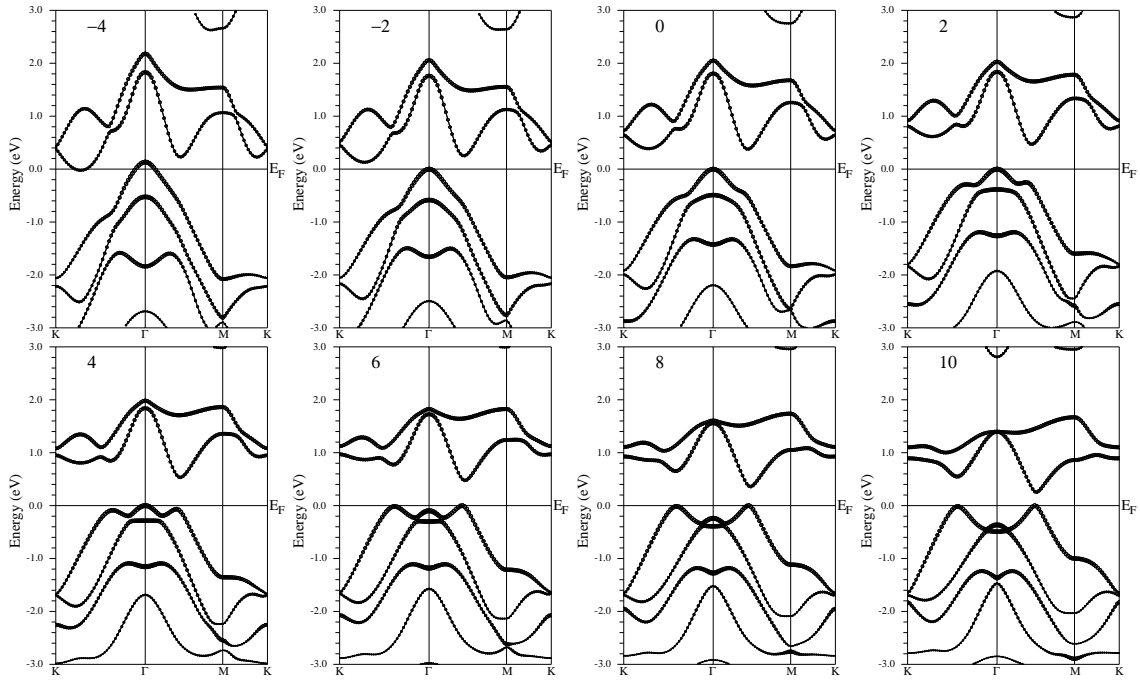


FIG. 2. The energy band structures of monolayer PtTe₂ with strain changing from -4% to 10% using GGA+SOC.

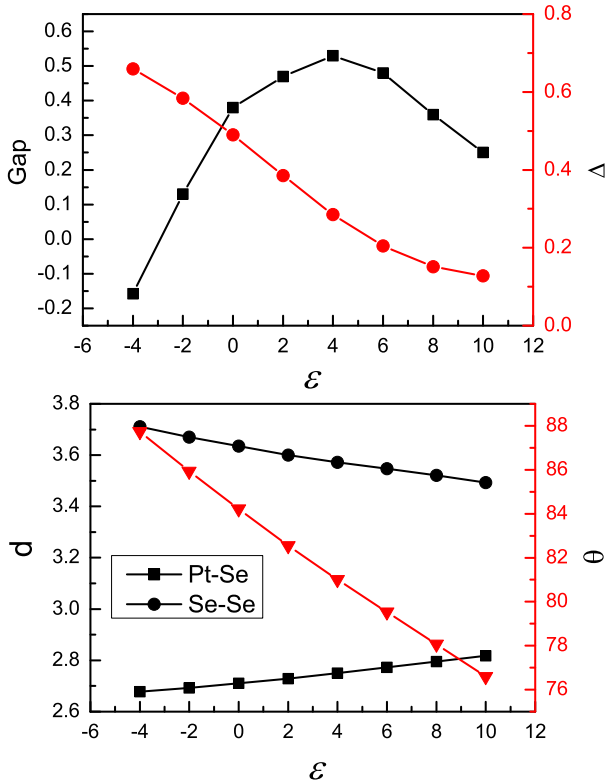


FIG. 3. (Color online) The energy band gap Gap (eV), the value of spin-orbit splitting at Γ point Δ (eV), Pt-Se and Se-Se bond lengths d (Å) and Se-Pt-Se bond angle Θ versus biaxial strain ϵ using GGA +SOC.

produce enhanced ZT_e . Tensile strain can also reduce lattice thermal conductivity, which has been found in monolayer PtSe₂²³ and ZrS₂²⁵. Therefore, tensile strain indeed can achieve enhanced thermoelectric properties.

The rest of the paper is organized as follows. In the next section, we shall give our computational details. In the third section, we shall present strain dependence of the electronic structures and thermoelectric properties of monolayer PtTe₂. Finally, we shall give our discussions and conclusions in the fourth section.

II. COMPUTATIONAL DETAIL

The first-principles calculations are carried out based on density functional theory²⁶ as implemented in the WIEN2k package²⁷ within the full-potential linearized augmented-plane-waves method. The GGA of Perdew, Burke and Ernzerhof (GGA-PBE)²⁸ is used as the exchange-correlation potential, including all the relativistic effects for electron part^{29–32}. The 6000 k-points are used in the first Brillouin zone (BZ) for the self-consistent calculation. The free atomic position parameters are optimized using GGA-PBE with a force standard of 2 mRy/a.u.. The harmonic expansion up to $l_{\max} = 10$ is used in each of the atomic spheres, and $R_{\text{mt}} * k_{\max} = 8$ is used to determine the plane-wave cutoff. The charge convergence criterion is used, and when the integration of the absolute charge-density difference between the input and output electron density is less than $0.0001|e|$ per formula unit, the self-consistent calculations are considered to be converged. Transport calculations are carried

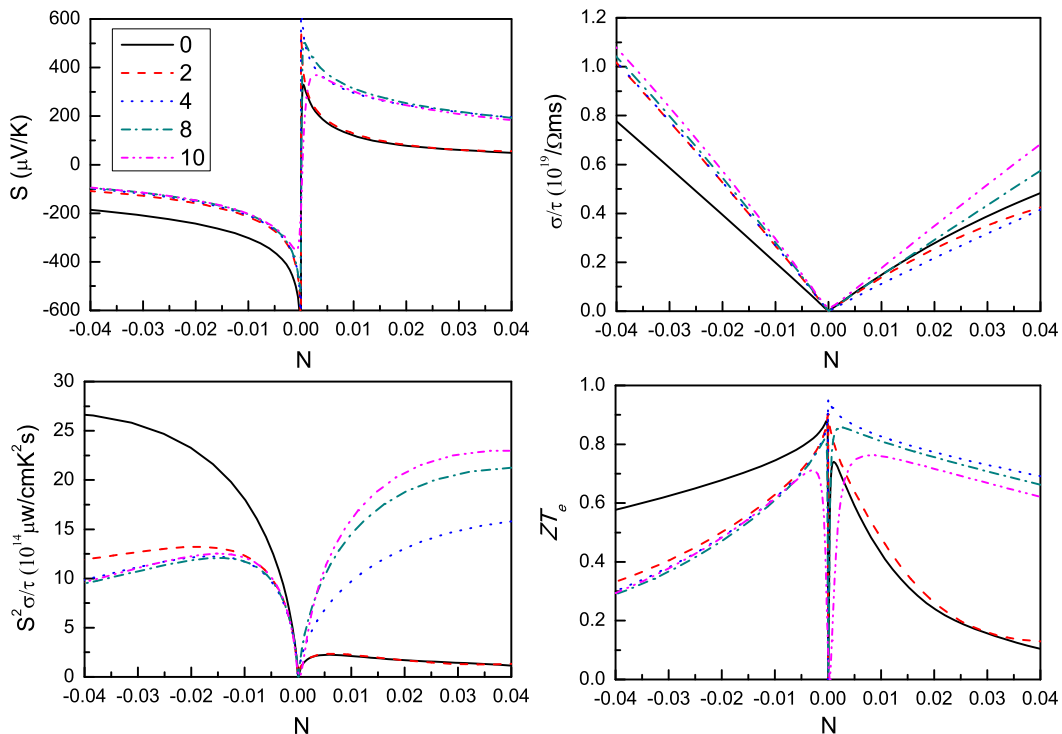


FIG. 4. (Color online) At room temperature, tensile strain dependence of Seebeck coefficient S , electrical conductivity with respect to scattering time σ/τ , power factor with respect to scattering time $S^2\sigma/\tau$ and upper limit of ZT_e versus doping level (N) using GGA+SOC.

out within the BoltzTrap code³³, which has been applied successfully to several materials^{34–36}. Since the accurate transport coefficients need sufficient k-points, the energy band structures are calculated using $65 \times 65 \times 11$ k-point meshes (50000 k-points) in the first Brillouin zone. For 2D materials, the parameter LPFAC usually should choose larger value. Here, we choose LPFAC value for 20 to achieve the convergence results. Phonon frequencies are obtained using the Phonopy code³⁷ using $5 \times 5 \times 1$ supercell with $8 \times 8 \times 1$ Monkhorst-Pack k meshes. The lattice thermal conductivities are calculated within the linearized phonon Boltzmann equation, which can be achieved by using Phono3py+VASP codes^{38–41}. The second order harmonic and third order anharmonic interatomic force constants are calculated by using a $4 \times 4 \times 1$ supercell and a $3 \times 3 \times 1$ supercell, respectively. To compute lattice thermal conductivities, the reciprocal spaces of the primitive cells are sampled using the $30 \times 30 \times 3$ meshes.

III. MAIN CALCULATED RESULTS AND ANALYSIS

The monolayer PtTe₂ is composed of three atomic sublayers with Pt sublayer sandwiched in two Te sublayers, and the schematic crystal structure is shown in Figure 1. The unit cell of monolayer PtTe₂ used in the calculations,

containing two Te and one Pt atoms, is constructed with the vacuum region of larger than 15 Å to avoid spurious interaction, and the optimized lattice constant is $a=4.02$ Å within GGA-PBE. It has been proved that SOC has important effects on both electronic structures and thermoelectric properties of semiconducting transition-metal dichalcogenide monolayers^{19,23,24}. Therefore, the GGA+SOC is employed to investigate strain dependence of electronic structures and thermoelectric properties in monolayer PtTe₂. The unstrained PtTe₂ is an indirect gap semiconductor of 0.38 eV gap value, with VBM at Γ point and CBM between Γ and M points, and the corresponding energy band structure is shown in Figure 2.

Both theoretically and experimentally, strain effects on the electronic structures of semiconducting transition-metal dichalcogenide monolayers have been widely studied^{13,17,19,22,23,25}, some of which are predicted to produce semiconductor-metal phase transition by applying suitable strain. The strain can be simulated by defining $\varepsilon = (a - a_0)/a_0$, where a_0 is the unstrained lattice constant optimized by GGA-PBE, with $\varepsilon < 0$ (> 0) being compressive (tensile) strain. The energy band structures of monolayer PtTe₂ with strain changing from -4% to 10% are plotted in Figure 2 using GGA+SOC. The energy band gap, spin-orbit splitting value at Γ point between the first and second valence bands, Pt-Se (Se-Se) bond length and Se-Pt-Se bond angle versus biaxial strain ε using GGA +SOC are shown in Fig-

ure 3. With strain changing from compressive one to tensile one, the energy band gap firstly increases, and then decreases, which has been found in many semiconducting transition-metal dichalcogenide monolayers, such as MoS₂^{17,19}, ZrS₂²⁵ and PtSe₂²³. It is noteworthy that small compressive strain (about -3%) can induce semiconductor-metal phase transition, which is less than critical strain of semiconductor-metal phase transition of other 2D materials^{17,22,25}. As the tensile strain increases, the CBM moves toward lower energy, while the VBM changes from the Γ point to the one along the Γ -M direction. When the VBM appears at one point along the Γ -M direction, the VBM and valence band extrema (VBE) along Γ -K direction are almost degenerate, which can give rise to important effect on Seebeck coefficient. With the increasing compressive strain, the CBM moves from the one point along the Γ -M direction to the one along the Γ -K direction. When the strain reaches about -3%, both VBM and CBM cross the Fermi level, inducing semiconductor-metal phase transition, which is due to enhanced orbital overlap and hybridization by reduced Pt-Se bond length. For MoS₂, the band gap is sensitively dependent on the S-S or Mo-S bond lengths and S-Mo-S bond angle⁴², the S-S bond length and S-Mo-S bond angle of which monotonously decrease with strain ($\leq \pm 10\%$) increasing, and the Mo-S bond length of which monotonously increases. Similarly, Se-Se bond length and Se-Pt-Se bond angle monotonously decrease with increasing strain considered in the calculations, and Pt-Se bond length monotonously increases. When the strain increases from -4% to 10%, the spin-orbit splitting at Γ point monotonically decreases from 0.66 eV to 0.13 eV. This trend of spin-orbit splitting versus strain is the same with one of monolayer PtSe₂²³, while it is opposite to one of MoS₂¹⁹.

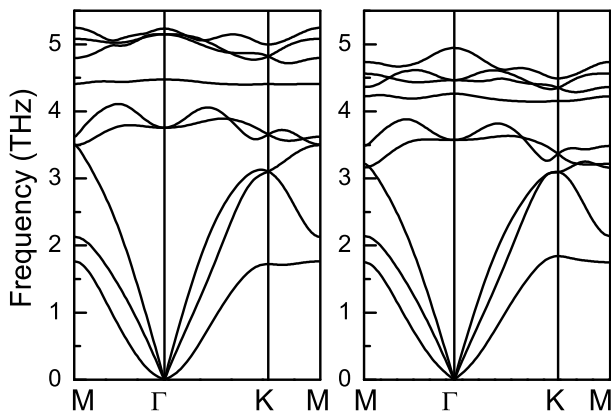


FIG. 5. Phonon band structure of PtTe₂ with strain being 0% (Left) and 4% (Right) using GGA-PBE.

As is well known, bands converge, including orbital and valley degeneracies, is a very effective strategy to improve Seebeck coefficient, and then to enhance power factor⁴³. The bands converge can be achieved by strain in many 2D materials such as MoS₂, PtSe₂ and black

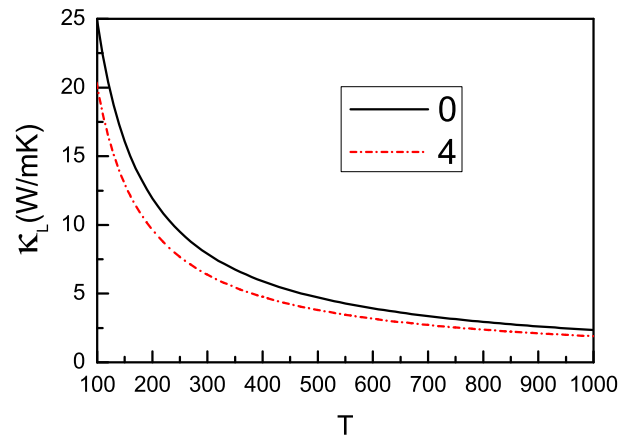


FIG. 6. (Color online) The lattice thermal conductivities of PtTe₂ with strain being 0% and 4% using GGA-PBE.

phosphorus^{19,23,44}. According to energy band structures with different strain in Figure 2, the unstrained PtSe₂ nearly has a valley degeneracy of 4 due to the convergence of two conduction band extrema (CBE) along the Γ -M and Γ -K directions, which produces largest n-type Seebeck coefficient (absolute value). Tensile strain can lead to the convergence of VBE along the Γ -M and Γ -K directions, which can lead to enhanced p-type Seebeck coefficient. Next, the transport coefficients are calculated based on the constant scattering time approximation (CSTA) Boltzmann theory within the rigid band approach, being effective for low doping level⁴⁵⁻⁴⁷. The n-type doping (negative doping level) with the negative Seebeck coefficient can be simulated by shifting the Fermi level into conduction bands, while the p-type doping (positive doping level) with positive Seebeck coefficient can be achieved by making Fermi level move into valence bands.

To address tensile strain enhanced power factor, the tensile strain dependence of Seebeck coefficient S , electrical conductivity with respect to scattering time σ/τ and power factor with respect to scattering time $S^2\sigma/\tau$ using GGA+SOC at room temperature are plotted in Figure 4. It is clearly seen that the unstrained PtTe₂ shows the largest n-type Seebeck coefficient, and that tensile strain can induce enhanced Seebeck coefficient. Calculated results show that the PtTe₂ with strain from 4% to 10% shows the nearly same Seebeck coefficient in high doping level. These can be explained by bands converge mentioned above. The complex strain dependence of electrical conductivity is observed, due to the sensitive dependence of energy band structures on the applied strain. For power factor combining Seebeck coefficient with electrical conductivity, the unstrained PtTe₂ has the highest n-type one, while the strain-improved p-type one increases from 4% to 10%. An upper limit of ZT , taking no account of lattice thermal conductivity, can be defined as $ZT_e = S^2\sigma T/\kappa_e$, whose tensile strain dependence for PtTe₂ is shown in Figure 4. The highest

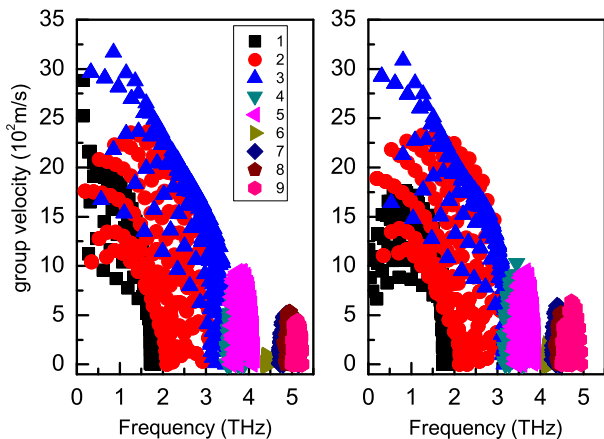


FIG. 7. (Color online) Calculated phonon group velocities of PtTe₂ with strain being 0% (Left) and 4% (Right) using GGA-PBE in the irreducible Brillouin zone.

n-type ZT_e is observed in unstrained PtTe₂, while the strain-improved p-type ZT_e in PtTe₂ with strain from 4% to 10% in high doping level is almost the same.

To further confirm tensile strain-enhanced p-type thermoelectric properties, the lattice thermal conductivities with strain being 0% and 4% are calculated. Phonon band structures of PtTe₂ with strain being 0% and 4% are plotted in Figure 5. It is found that the longitudinal acoustic (LA) and transverse acoustic (TA) branches of PtTe₂ with strain being 0% and 4% are linear near the Γ point, while the z-direction acoustic (ZA) branch is quadratic near the Γ point. The dispersion of the ZA branch with strain being 4% becomes more linear than unstrained one in the long-wavelength limit. Calculated results also show that the optical branch with strain being 4% moves toward lower energy compared to unstrained one. Thermal conductivity is an intensive property for bulk materials⁴⁸. The calculated thermal conductivities for 2D materials should be normalized by multiplying Lz/d , where Lz is the length of unit cell along z direction, including vacuum region, and d is the thickness of 2D materials. However, the thickness of 2D materials is not well defined. To only prove tensile strain-reduced lattice thermal conductivity, the unnormalized lattice thermal conductivities with strain being 0% and 4% are shown in Figure 6. Calculated results show that the lattice thermal conductivity ($6.37 \text{ Wm}^{-1}\text{K}^{-1}$) at the strain of 4% can decrease by about 19% compared to unstrained one ($7.89 \text{ Wm}^{-1}\text{K}^{-1}$) at 300 K. The group velocities in the irreducible BZ with nine different bands are plotted in Figure 7. It is found that the group velocities of the first band with strain being 4% become more lower than unstrained one, which leads to lower lattice thermal conductivities. Similar tensile strain-reduced κ_L has also been proved in monolayer PtSe₂²³ and ZrS₂²⁵ by the first-principles calculations. To compare the lattice thermal conductivities of different 2D materials, the same

thickness d should be used⁴⁸. The room-temperature lattice conductivity of PtTe₂ ($7.89 \text{ Wm}^{-1}\text{K}^{-1}$ with Lz being 20.12 \AA) is lower than one of PtSe₂ ($16.97 \text{ Wm}^{-1}\text{K}^{-1}$ with Lz being also 20.12 \AA) because of larger lattice constants a ²³. Considering tensile strain-enhanced ZT_e and -reduced κ_L , tensile strain indeed can improve the efficiency of thermoelectric conversion.

IV. DISCUSSIONS AND CONCLUSION

PtTe₂ possesses the smallest gap among the PtX₂ (X=S, Se and Te) monolayers²⁴, and a semiconductor-to-metal transition can easily be produced for PtTe₂ by strain tuning. Calculated results show that about -3% compressive strain can induce semiconductor-to-metal transition, which is lower than the critical strain of MoS₂ (about 10% tensile strain and 15% compressive strain)¹⁷ and ZrS₂ (about 8% compressive strain)²⁵. Experimentally, such a small strain can easily be achieved by piezoelectric stretching and exploiting the thermal expansion mismatch^{49,50}.

The conduction bands converge for unstrained PtTe₂ naturally exists, which is in favour of better n-type thermoelectric performance (See Figure 4). Both compressive and tensile strain can remove conduction bands converge, but tensile strain can induce valence bands converge, which is in support of better p-type thermoelectric properties. Calculated results show that tensile strain not only can enhance ZT_e , but also can reduce κ_L , which implies that tensile strain indeed can improve the efficiency of thermoelectric conversion of PtTe₂. Similar strain-enhanced thermoelectric properties also can be found in monolayer MoS₂¹⁹, PtSe₂²³ and ZrS₂²⁵.

In summary, we investigate strain dependence of electronic structures and thermoelectric properties of monolayer PtTe₂ based mainly on the reliable first-principle calculations and Boltzmann transport theory. Calculated results show that small compressive strain can give rise to semiconductor-to-metal transition. It is found that tensile strain can enhance ZT_e and reduce lattice thermal conductivity, and then improve the efficiency of thermoelectric conversion of PtTe₂. So, strain is a very effective method to achieve tuned electronic and thermoelectric properties of monolayer PtTe₂, which provides great opportunities for applications in electronics and thermoelectricity.

ACKNOWLEDGMENTS

This work is supported by the National Natural Science Foundation of China (Grant No. 11404391). We are grateful to the Advanced Analysis and Computation Center of CUMT for the award of CPU hours to accomplish this work.

-
- ¹ A. C. Ferrari, F. Bonaccorso et al., *Nanoscale* **7**, 4598 (2015).
- ² K. S. Novoselov, V. I. Fal'ko, L. Colombo, P. R. Gellert, M. G. Schwab, and K. Kim, *Nature* **490**, 192 (2012).
- ³ Q. H. Wang, K. Kalantar-Zadeh, A. Kis, J. N. Coleman and M. S. Strano, *Nature Nanotechnology* **7**, 699 (2012).
- ⁴ M. S. Xu, T. Liang, M. M Shi and H. Z. Chen, *Chem. Rev.* **113** 3766 (2013).
- ⁵ L. Song, L. J. Ci, H. Lu et al., *Nano Lett.* **10**, 3209 (2010).
- ⁶ Z. Y. Ni, Q. H. Liu, K. C. Tang et al., *Nano Lett.* **12**, 113 (2012).
- ⁷ H. Liu, A. T. Neal, Z. Zhu et al., *ACS Nano* **8**, 4033 (2014).
- ⁸ L. Li, Z. Chen, Y. Hu et al., *J. Am. Chem. Soc.* **135**, 1213 (2013).
- ⁹ Q. H. Wang, K. Kalantar-Zadeh, A. Kis, J. N. Coleman and M. S. Strano, *Nature Nanotechnology* **7**, 699 (2012).
- ¹⁰ K. F. Mak, C. Lee, J. Hone, J. Shan, and T. F. Heinz, *Phys. Rev. Lett.* **105**, 136805 (2010).
- ¹¹ S. Ghatak, A. N. Pal and A. Ghosh, *Acs Nano* **5**, 7707 (2011).
- ¹² B. Radisavljevic, A. Radenovic, J. Brivio, V. Giacometti and A. Kis, *Nature Nanotechnology* **6**, 147 (2011).
- ¹³ S. Bhattacharyya, T. Pandey and A. K. Singh, *Nanotechnology* **25**, 465701 (2014).
- ¹⁴ K. X. Chen, X. M. Wang, D. C. Mo and S. S. Lyu, *J. Phys. Chem. C* **119**, 26706 (2015).
- ¹⁵ M. Tahir and U. Schwingenschlögl, *New Journal of Physics* **16**, 115003 (2014).
- ¹⁶ A. Arab and Q. Li, *Sci. Rep.* **5**, 13706 (2015)
- ¹⁷ E. Scalise, M. Houssa, G. Pourtois, V. Afanas'ev and A. Stesmans, *Nano Res.* **5**, 43 (2012).
- ¹⁸ H. Peelaers and C. G. Van de Walle, *Phys. Rev. B* **86**, 241401(R) (2012).
- ¹⁹ S. D. Guo, *Comp. Mater. Sci.* **123**, 8 (2016).
- ²⁰ Y. L. Wang et al. *Nano Lett.* **15**, 4013 (2015).
- ²¹ W. Yao et al. arXiv:1603.02140.
- ²² P. F. Li, L. Li and X. C. Zeng, *J. Mater. Chem. C*, **4**, 3106 (2016).
- ²³ S. D. Guo, *J. Mater. Chem. C* **4**, 9366 (2016).
- ²⁴ S. D. Guo and J. L. Wang, *Semicond. Sci. Tech.* **31**, 095011 (2016).
- ²⁵ H. Y. Lv, W. J. Lu, D. F. Shao, H. Y. Lub and Y. P. Sun, *J. Mater. Chem. C* **4**, 4538 (2016).
- ²⁶ P. Hohenberg and W. Kohn, *Phys. Rev.* **136**, B864 (1964); W. Kohn and L. J. Sham, *Phys. Rev.* **140**, A1133 (1965).
- ²⁷ P. Blaha, K. Schwarz, G. K. H. Madsen, D. Kvasnicka and J. Luitz, WIEN2k, an Augmented Plane Wave + Local Orbitals Program for Calculating Crystal Properties (Karlheinz Schwarz Technische Universität Wien, Austria) 2001, ISBN 3-9501031-1-2
- ²⁸ J. P. Perdew, K. Burke and M. Ernzerhof, *Phys. Rev. Lett.* **77**, 3865 (1996).
- ²⁹ A. H. MacDonald, W. E. Pickett and D. D. Koelling, *J. Phys. C* **13**, 2675 (1980).
- ³⁰ D. J. Singh and L. Nordstrom, *Plane Waves, Pseudopotentials and the LAPW Method*, 2nd Edition (Springer, New York, 2006).
- ³¹ J. Kunes, P. Novak, R. Schmid, P. Blaha and K. Schwarz, *Phys. Rev. B* **64**, 153102 (2001).
- ³² D. D. Koelling, B. N. Harmon, *J. Phys. C: Solid State Phys.* **10**, 3107 (1977).
- ³³ G. K. H. Madsen and D. J. Singh, *Comput. Phys. Commun.* **175**, 67 (2006).
- ³⁴ B. L. Huang and M. Kaviani, *Phys. Rev. B* **77**, 125209 (2008).
- ³⁵ L. Q. Xu, Y. P. Zheng and J. C. Zheng, *Phys. Rev. B* **82**, 195102 (2010).
- ³⁶ J. J. Pulikkotil, D. J. Singh, S. Auluck, M. Saravanan, D. K. Misra, A. Dhar and R. C. Budhani, *Phys. Rev. B* **86**, 155204 (2012).
- ³⁷ A. Togo and I. Tanaka, *Scr. Mater.* **108**, 1 (2015).
- ³⁸ G. Kresse, *J. Non-Cryst. Solids* **193**, 222 (1995).
- ³⁹ G. Kresse and J. Furthmüller, *Comput. Mater. Sci.* **6**, 15 (1996).
- ⁴⁰ G. Kresse and D. Joubert, *Phys. Rev. B* **59**, 1758 (1999).
- ⁴¹ A. Togo, L. Chaput and I. Tanaka, *Phys. Rev. B* **91**, 094306 (2015).
- ⁴² X. G. Liu and Z. Y. Li, *J. Phys. Chem. Lett.* **6**, 3269 (2015).
- ⁴³ Y. Pei, X. Shi, A. LaLonde, H. Wang, L. Chen and G. J. Snyder, *Nature* **473**, 66 (2011).
- ⁴⁴ G. Z. Q. B. Yan et al., *Sci. Rep.* **4**, 6946 (2014).
- ⁴⁵ T. J. Scheideman, C. Ambrosch-Draxl, T. Thonhauser, J. V. Badding and J. O. Sofo, *Phys. Rev. B* **68**, 125210 (2003).
- ⁴⁶ G. K. H. Madsen, *J. Am. Chem. Soc.* **128**, 12140 (2006).
- ⁴⁷ X. Gao, K. Uehara, D. Klug, S. Patchkovskii, J. Tse and T. Tritt, *Phys. Rev. B* **72**, 125202 (2005).
- ⁴⁸ X. F. Wu, V. Varshney et al., arXiv:1607.06542 (2016).
- ⁴⁹ Y. Y. Hui et al. *ACS Nano* **7**, 7126 (2013).
- ⁵⁰ G. Plechinger et al. *2D Mater.* **2**, 015006 (2015).